Accepted Manuscript

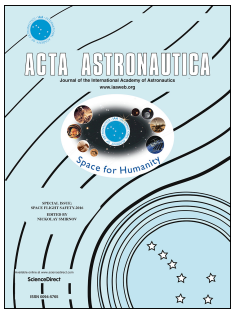

Onboard guidance system design for reusable launch vehicles in the terminal area energy management phase

Lingxia Mu, Xiang Yu, Youmin Zhang, Ping Li, Xinmin Wang

PII: S0094-5765(17)30548-9

DOI: 10.1016/j.actaastro.2017.10.027

Reference: AA 6517

To appear in: *Acta Astronautica*

Received Date: 18 April 2017

Revised Date: 29 July 2017

Accepted Date: 21 October 2017

Please cite this article as: L. Mu, X. Yu, Y. Zhang, P. Li, X. Wang, Onboard guidance system design for reusable launch vehicles in the terminal area energy management phase, *Acta Astronautica* (2017), doi: 10.1016/j.actaastro.2017.10.027.

Onboard Guidance System Design for Reusable Launch Vehicles in the Terminal Area Energy Management Phase

Lingxia Mu[a,b], Xiang Yu[b], Youmin Zhang[b,1], Ping Li[a], Xinmin Wang[a]

[a]*School of Automation, Northwestern Polytechnical University, Xi'an 710072, China*
[b]*Department of Mechanical, Industrial, and Aerospace Engineering, Concordia University, Montreal H3G 1M8, Canada*

Abstract

A terminal area energy management (TAEM) guidance system for an unpowered reusable launch vehicle (RLV) is proposed in this paper. The mathematical model representing the RLV gliding motion is provided, followed by a transformation of extracting the required dynamics for reference profile generation. Reference longitudinal profiles are conceived based on the capability of maximum dive and maximum glide that a RLV can perform. The trajectory is obtained by iterating the motion equations at each node of altitude, where the angle of attack and the flight-path angle are regarded as regulating variables. An onboard ground-track predictor is constructed to generate the current range-to-go and lateral commands online. Although the longitudinal profile generation requires pre-processing using the RLV aerodynamics, the ground-track prediction can be executed online. This makes the guidance scheme adaptable to abnormal conditions. Finally, the guidance law is designed to track the reference commands. Numerical simulations demonstrate that the proposed guidance scheme is capable of guiding the RLV to the desired touchdown conditions.

Keywords:

Terminal area energy management (TAEM), Guidance system, Trajectory planning, Ground-track predictor, Reusable launch vehicle (RLV)

1. Introduction

The second-generation reusable launch vehicles (RLVs) have been designed, aiming at reducing the costs of space transportation while improving the safety and reliability of the vehicles [1], [2]. Advanced guidance and control (G&C) technologies are well recognized as an effective means to achieve these objectives particularly during reentry flight [3]. The atmospheric reentry of a RLV usually starts with an initial reentry (IRE) phase, followed by a terminal area energy management (TAEM) phase as well as an approach and landing (A&L) phase.

As far as the TAEM guidance is concerned, the objective is to guide the unpowered RLV from a terminal entry point (TEP) with a given energy state to an expected approach and landing interface (ALI) without violating the vehicle's design constraints (e.g., the dynamic pressure and the load factor). It is characterized by a heading alignment cylinder (HAC), during which the RLV performs a turn around the cylinder to align with the runway.

[1] Correspondence to: Department of Mechanical, Industrial, and Aerospace Engineering, Concordia University, 1455 de Maisonneuve Boulevard West, Montreal, Quebec H3G 1M8, Canada. E-mail address: youmin.zhang@concordia.ca

This feature of lateral manoeuver makes the TAEM phase significantly different from the IRE phase and A&L phase in three dimensional motions. Recently, extensive studies focus on guidance scheme for vertical motion in IRE and A&L phases, such as [4], [5], [6], [7], [8], and [9], nevertheless fewer efforts have been placed on the TAEM guidance scheme.

The preliminary TAEM guidance system in the US space shuttle relies on reference trajectories that are calculated and stored in the onboard computer before flight [10]. This strategy works well in nominal cases. However, the offline trajectories with decoupled lateral and longitudinal channels can result in some limitations. 1) The capability of accommodating large uncertainties is limited due to fixed reference trajectories. 2) The accuracy of terminal guidance is decreased as a consequence of the decoupling between lateral and longitudinal motions.

To address the aforementioned issues, several efforts have been devoted to online guidance systems for the TAEM phase. An onboard two-dimensional trajectory planning algorithm is developed in [11] and [12]. The main idea is to generate a feasible path by iterating three geometric parameters. The ground-track path is firstly designed, followed by an altitude profile conceived as a function of ground-track range. Feasible trajectories are therefore constructed by propagating the energy from the TEP to the ALI. Finally the best one is selected according to the cost function. In [13] and [14], the energy-tube concept is introduced to analyze the maximum and minimum required energies for a specific target point. Afterwards this concept is integrated into a planning and estimation algorithm to calculate the best HAC position, as well as its deviation in response to abnormal conditions [15]. In [16], a long-term and short-term online trajectory generation scheme is proposed, accounting for the most relevant vehicle and trajectory constraints. In [17], an online trajectory planning and guidance approach is proposed, where the reference path can be adjusted online. The guidance adaptation capability is improved by these strategies to some extent. The reference longitudinal profile in these methods is usually defined by an altitude profile as a quadratic polynomial of ground-track range or a Mach profile as a cubic polynomial of altitude. However, the physical interpretation of such a longitudinal profile requires more explanations, taking [16] as example. On the other hand, it might be impossible to use a single fixed longitudinal profile in the event of off-nominal conditions, which is also concluded in [13] and [17]. Hence, further investigation is needed for reference longitudinal profile design.

On the other hand, three-dimensional trajectory planning methods are discussed by considering the coupling between longitudinal and lateral motions. Offline three-dimensional trajectory planning algorithms are presented in [18] and [19]. However, a possible problem is that the maximum turning capability of the vehicle is always utilized, which limits the capability of adjusting the trajectory under abnormal conditions. Other studies have focused on applying direct non-linear programming (NLP) to the TAEM guidance problem. For example, a NLP optimizer is exploited for trajectory planning, allowing for the restrictions of mission profile and off-nominal conditions [20]. A three-dimensional TAEM trajectory planning algorithm combined with a down-track correction scheme is proposed in [21]. In [22], an adaptive neural network-based methodology is studied to maintain a gradual glideslope and meet specific constraints, where the cost function is formulated. A new trajectory optimization algorithm is presented based on interval analysis in [23]. An optimization algorithm with dynamic pressure as the cost function is used to

obtain the optimal trajectory for TAEM phase [24]. The NLP-based trajectory planning strategies using the theory of differential flatness are investigated in [25] and [26]. These NLP-based three-dimensional trajectory planning algorithms can generate trajectories precisely. However, they are usually time-consuming for onboard applications. In addition, little attention has been paid on the unique feature of the unpowered gliding motion in these algorithms.

Motivated by the discussed facts, this paper focuses on an onboard TAEM guidance system design. The developed scheme generates longitudinal profiles by taking into consideration of the vehicle dynamic constraints. Meanwhile, the ground-track path is adjusted in real-time, and the guidance commands are generated online. In such a way, this scheme is adaptable in the event of variations in initial conditions, and might potentially serve as an onboard guidance scheme. Compared with the existing literature, the contributions of this paper lie in four aspects. 1) A dynamic pressure profile with explicit physical interpretation is conceived by iterating the kernel extraction protocol (KEP) equations; 2) An onboard task management scheme is constructed to predict ground-track range online. Guidance commands are generated subsequently by comparing the predicted range with the reference one. In this way, the longitudinal and lateral motions are combined together; 3) A guidance law with consideration of real flight situations is developed for trajectory tracking; 4) Simulations with consideration of not only initial condition variations but also model uncertainties are conducted to verify the feasibility and robustness of the proposed method.

The rest of the paper is arranged as follows. Section 2 presents the mathematical model and KEP equations, as well as the idea of energy management and TAEM guidance objectives. In Section 3, the dynamic pressure profiles bounded by maximum dive and maximum glide capability is proposed. In Section 4, an onboard ground-track predictor (GTP) is developed. In Section 5, the guidance laws for both longitudinal and lateral motions are investigated. In Section 6, the effectiveness of the proposed guidance scheme is demonstrated by simulating different TAEM scenarios in the presence of abnormal conditions. Concluding remarks are drawn in Section 7.

2. Preliminaries

2.1. Mathematical Model

By assuming a flat Earth, three-dimensional gliding dynamics of an unpowered RLV during the TAEM phase can
be described as:

$$\frac{dV}{dt} = -\frac{D}{m} - g\sin\gamma, \tag{1}$$

$$\frac{d\gamma}{dt} = \frac{L\cos\mu}{mV} - \frac{g}{V}\cos\gamma, \tag{2}$$

$$\frac{d\psi}{dt} = \frac{L\sin\mu}{mV\cos\gamma}, \tag{3}$$

$$\frac{dx}{dt} = V\cos\gamma\cos\psi, \tag{4}$$

$$\frac{dy}{dt} = V\cos\gamma\sin\psi, \tag{5}$$

$$\frac{dh}{dt} = Vsin\gamma, \tag{6}$$

where V is the velocity, γ is the flight-path angle, ψ is the heading angle, x is the down-track position along runway centerline, y is the cross-track position from runway centerline, h is the altitude, μ is the bank angle, m is the mass, and g is the constant gravitational acceleration. The lift force L and drag force D are calculated as:

$$L = \bar{q}S_{ref}C_L, \tag{7}$$

$$D = \bar{q}S_{ref}C_D, \tag{8}$$

with the dynamic pressure $\bar{q}$ defined by:

$$\bar{q} = 0.5\rho V^2, \tag{9}$$

where S_{ref} is the reference area, and ρ is the atmospheric density. The lift coefficient C_L and the drag coefficient C_D are depended on angle of attack α, Mach number M, and speedbrake deflection δ_{sb}. Note that a speedbrake is modeled as an aerodynamic drag increment, which is initiated during subsonic flight in this work. Moreover, control surface positions (i.e., aileron, body-flap, elevator, and rudder) have impacts on C_L and C_D, as a matter of fact. They are ignored nevertheless for the sake of simplicity, since the neglected terms affect primarily rotational motion rather than point-mass motion.

2.2. KEP Equations

It is a traditional way for trajectory planning to integrate the motion equations (1)-(6) in the time domain. However, motivated by [18], the KEP motion equations are derived in this section and used to generate reference trajectory hereafter. The KEP equations are essentially rearrangements of the motion equations into a form involving dynamic pressure and altitude. To this end, taking the derivative of Eq. (9) with respect to time, and recalling Eq. (6) , one can get:

$$\frac{d\bar{q}}{dt} = \rho V\dot{V} + 0.5\dot{\rho}V^2 = \frac{\rho}{sin\gamma}\frac{dh}{dt}\frac{dV}{dt} + \frac{d\rho}{dt}\frac{\bar{q}}{\rho}. \tag{10}$$

Then, in order to replace time with altitude as the independent variable, dividing Eq. (10) by Eq. (6) yields an expression for change rate of dynamic pressure with respect to altitude:

$$\frac{d\bar{q}}{dh} = \frac{\rho}{sin\gamma}\frac{dV}{dt} + \frac{d\rho}{dh}\frac{\bar{q}}{\rho}. \tag{11}$$

By substituting Eq. (1) into Eq. (11), and recalling the definition of drag force from Eq. (8), Eq. (11) is rewritten as:

$$\frac{d\bar{q}}{dh} = \left(\frac{1}{\rho}\frac{d\rho}{dh} - \frac{\rho S_{ref}C_D}{msin\gamma}\right)\bar{q} - \rho g, \tag{12}$$

where $\frac{d\rho}{dh}$ can be extracted from an atmospheric model. The similar transformation is made to Eq. (2), achieving:

$$\frac{d\gamma}{dh} = \frac{\rho}{2sin\gamma}\left(\frac{S_{ref}C_L cos\mu}{m} - \frac{gcos\gamma}{\bar{q}}\right). \tag{13}$$

Additionally, the ground-track range R is defined as:

$$\frac{dR}{dt} = Vcos\gamma, \tag{14}$$

Then, the expression of the ground-track range with respect to altitude can be obtained using the chain rule:

$$\frac{dR}{dh} = \frac{dR}{dt}\frac{dt}{dh} = \frac{1}{tan\gamma}. \tag{15}$$

Remark 1. Different from the conventional equations of motion (1)-(6), altitude h and dynamic pressure $\bar{q}$ in the KEP equations are considered as independent variable and state variable, respectively. In fact, these KEP equations extract the main characters of RLV's gliding motion in three aspects: 1) Velocity is replaced with $\bar{q}$ as a guidance state since $\bar{q}$ is directly imposed on constraints during reentry flights; 2) As a much more slowly varying parameter, $\bar{q}$ provides with a more robust iteration on the nonlinear equations of motion; and 3) Altitude is employed as an independent variable due to that one is usually interested in a successful gliding at a predetermined and fixed altitude instead of a fixed time in practical TAEM flights.

In summary, these features make the KEP equations more efficient in generating trajectory based on the domain of altitude. The KEP equations will be used in Section 3 for reference longitudinal profiles generation.

2.3. The Concept of Energy Management

The main goal of TAEM phase is to regulate the energy, including potential and kinetic energy, such that the unpowered RLV can arrive at ALI with an appropriate amount of energy. Hence, a significant indicator to measure the RLV's energy is introduced herein, i.e., the energy over weight E_W (energy height). The definition is:

$$E_W = h + \frac{V^2}{2g} = h + \frac{\bar{q}}{\rho g}. \tag{16}$$

It can be seen from Eq. (16) that E_W captures both the potential and kinetic energy contributions in a single summation. It also indicates that the total energy is completely determined by the altitude and dynamic pressure. From this perspective, the energy can be managed as long as the altitude and velocity are controlled as expected. However, the TAEM flight is in fact a dynamic process and it is of great importance to guide the RLV to a specified landing interface. Thus, the range-to-go and lateral manoeuver has to be explicitly considered as well.

To this end, the rate of energy dissipation versus range-to-go is presented. By taking the derivative of E_W with respect to ground-track range, and using the chain rule, one can obtain:

$$\frac{dE_W}{dR} = \frac{dE_W}{dt}\frac{dt}{dR} = \frac{d\left(h+\frac{V^2}{2g}\right)}{dt}\frac{dt}{dR} = \frac{dh}{dR} + \frac{V\dot{V}}{g}\frac{dt}{dR}. \tag{17}$$

Substituting Eqs. (1), (14), and (15) into Eq. (17) gives the relational expression between the energy dissipation and the specific states:

$$\frac{dE_W}{dR} = tan\gamma - \frac{V}{g}\left(\frac{D}{m} + gsin\gamma\right)\frac{1}{Vcos\gamma} = -\frac{D}{mgcos\gamma}. \tag{18}$$

Table 1: TAEM guidance requirement

	Condition	Constraints
Design constraints	Normal acceleration	[-1, 1]
	Dynamic pressure, psf	[110, 400]
Kinematic constraints	Dynamic pressure at ALI, psf	255
	Altitude at ALI, ft	10,000
	Cross-track position at ALI, ft	0
	Down-track position at ALI, ft	0
	Heading angle at ALI, deg	0
	Flight path angle at ALI, deg	-9

Equation (18) shows that the rate at which the energy dissipates with the glide range is proportional to the drag and flight-path angle

As aforementioned, the energy can be dissipated by adjusting the change rate of energy dissipation in the vertical motion and the ground-track range in the lateral maneuver. In consequence, the problems of longitudinal trajectory generation and ground-track range prediction will be addressed in Section 3 and Section 4, respectively.

2.4. Problem Formulation

In general, the design goal of TAEM guidance system is to bring the unpowered RLV from the end of the IRE phase, i.e., TEP (when velocity reaches at the altitude of around 100; 000 $f\,t$ and Mach 3) to the ALI (nominally at the altitude of 10; 000 $f\,t$ and Mach 0:5). Meanwhile, TAEM guidance system is asked for aligning the RLV with the extended runway centerline, thus enabling a safe auto-landing hereafter.

During this process, the guidance system has to meet two kinds of requirements: 1) vehicle design constraints, essentially the load factor and the dynamic pressure, and 2) final constraints at ALI, namely, constraints on dynamic pressure, flight path, and heading angle. The ALI altitude is $h_{ALI} = 10{,}000ft$, and the location of ALI is fixed at $x_{ALI} = y_{ALI} = 0ft$. The desired dynamic pressure for ALI is $\bar{q}_{ALI} = 255psf$ (i.e., $V_{ALI} = \frac{539ft}{s}, M = 0.5$). Focusing on the studied RLV, the flight-path angle constraint of $-9deg$ at the ALI is chosen due to the quasi-equilibrium glide for dynamic pressure of $255psf$ with $d\bar{q}/dh$ of zero at $10{,}000ft$. All these requirements are presented in Table 1.

Therefore, on the basis of these requirements, a scheme of onboard TAEM guidance is developed in Fig. 1. The framework of the proposed TAEM guidance system mainly consists of three units. The first unit is to generate longitudinal reference trajectory which is described in Section 3. In the second unit, the ground-track predictor described in Section 4 is included. Integrated by a flight phase management module for different phases switching, TAEM task management is realized. Then the trajectory commands are generated including altitude, velocity,

heading angle, and bank angle. The third one is to effectively track the trajectory where a guidance law and necessary state transformation are required. Meanwhile, the assumption of time delay for the further control system is considered as well. The proposed TAEM guidance strategy can be achieved by following steps:

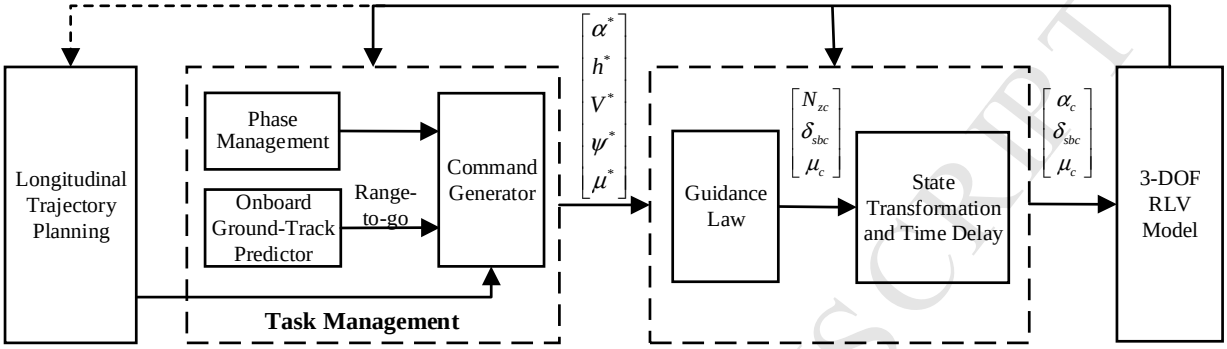

Fig. 1: The scheme of the proposed TAEM guidance system

Step 1

(a) Design reference dynamic pressure versus altitude profiles according to gliding capability of the vehicle.

(b) Generate reference trajectory parameters by the proposed TAEM trajectory iteration algorithm and record all trajectories as a database.

Step 2

(a) Predict a RLV's total range-to-go R_{total} according to the principle of ground-track predictor at the terminal entry point. Select which longitudinal profile a RLV should track by comparing the predicted R_{total} with the reference maximum range-to-go in the database generated by Step 1-(b).

(b) Predict range-to-go R_{tg} at each point on the path in real-time by onboard GTP. Correspondingly, reference longitudinal trajectory parameters (α^*, h^*, V^*) at each point on the path can be obtained by the lookup table. Meanwhile, the reference lateral trajectory parameters (ψ^*, μ^*) can be achieved by GTP.

Step 3

Track the reference trajectory by control commands $(\alpha_c, \delta_{sbc}, \mu_c)$ based on the designed guidance law.

Remark 2. As described in Step 2-(a), the total range-to-go R_{total} of the vehicle can be predicted according to the principle of GTP at the terminal entry point. Then, by comparing R_{total} with the maximum range-to-go in the database, a closest reference trajectory is selected. Note that the range-to-go in the database is obtained according to the specific dynamic pressure versus altitude profile. Thus, the chosen reference profile can result in the proper range, which ultimately matches the GTP range-to-go. By this means, the longitudinal and lateral motions are combined together.

3. Longitudinal Trajectory Generation

In this section, the objective is to 1) characterize an explicit longitudinal profile, i.e., dynamic pressure as a function of altitude; and 2) calculate the corresponding states history by an iterative algorithm. Firstly, dynamic pressure profile describing longitudinal features of a RLV is defined prior to trajectory generation, within the following constraints.

1) The initial and final boundary constraints on dynamic pressure are $\bar{q}_0(h_0) = \bar{q}_{TEP}$ and $\bar{q}_f(h_f) = \bar{q}_{ALI}$, respectively.

2) The dynamic pressure varies as smoothly as possible throughout the TAEM glide phase. The dynamic pressure keeps a small change rate in order for the approximate quasi-equilibrium glide (QEG)" (see [6] for details) during TAEM, and attains zero change rate at the end of TAEM, i.e., $(d\bar{q}/dh)_{ALI} = 0$, to ensure a QEG at A&L phase.

3) In addition, the dynamic pressure is bounded by the maximum value $\bar{q}_{\max}$ and the minimum value $\bar{q}_{\min}$.

Regarding the third constraint on dynamic pressure, the maximum dynamic pressure $\bar{q}_{\max}$ is set to protect the vehicle from any physical damages. Meanwhile, it also represents the maximum dive capability of the unpowered RLV. On the other hand, the minimum dynamic pressure $\bar{q}_{\min}$ is selected to represent the maximum glide capability of the unpowered RLV. Usually, a RLV can achieve the maximum range (or max glide) by flying at the maximum L/D ratio. However, when flying at the maximum L/D ratio, system states including α, γ, and $\bar{q}$ may suffer from undesirable chattering issues. In order to eliminate chattering issues, a constant dynamic pressure profile, which allows for a smoother trajectory, is expected to approximately replace the maximum L/D ratio profile. Hence, $\bar{q}_{\min}$ is found in this paper to represent a RLV's maximum glide capability.

According to the above analysis, a constant dynamic pressure profile is preferable. However, by taking the first constraint on initial and final $\bar{q}$ into consideration, a piecewise dynamic pressure profile is more practical. In addition, due to the fact that the second constraint is on the change rate of the dynamic pressure, it can be easier to design the $\bar{q}$ profile by starting from shaping its change rate. Hence, a profile of the dynamic pressure's change rate is firstly established including three segments. The middle segment equals to zero for a constant $\bar{q}_C$ flight, whilst the other two portions make use of the quadratic function (see Eq. (19)) to ensure the continuity between two prescribed dynamic pressures.

$$\frac{d\bar{q}}{dh}(h) = \begin{cases} a_{11}(h - a_{12})^2 + a_{13}, & h_{M1} \le h \le h_{TEP} \\ 0, & h_{M2} < h < h_{M1} \\ a_{21}(h - a_{22})^2 + a_{23}, & h_{ALI} \le h \le h_{M2} \end{cases}, \tag{19}$$

where h_{ALI} and h_{TEP} are altitude at the ALI and TEP respectively. $[h_{M2}, h_{M1}]$ describes altitude range where constant dynamic pressure is expected for a RLV. $a_{ij}|_{i=1,2;j=1,2,3}$ are parameters to be determined by the constraints on altitude and dynamic pressure (and its changing rate) at a specific point.

Initial, middle, and finial dynamic pressures are denoted by $\bar{q}_{TEP}$, $\bar{q}_C$, and $\bar{q}_{ALI}$, respectively. Integrating Eq. (19) along the altitude achieves dynamic pressure profile:

$$\bar{q}(h) = \begin{cases} \bar{q}_{TEP} + \frac{a_{11}}{3}[(h-a_{12})^3 - (h_{TEP}-a_{12})^3] + a_{13}(h-h_{TEP}), & h_{M1} \le h \le h_{TEP} \\ \bar{q}_C, & h_{M2} < h < h_{M1} \\ \bar{q}_C + \frac{a_{21}}{3}[(h-a_{22})^3 - (h_{M2}-a_{22})^3] + a_{23}(h-h_{M2}), & h_{ALI} \le h \le h_{M2} \end{cases}. \quad (20)$$

Regarding the parameters in Eq. (19), firstly, according to definition of h_{TEP} and h_{M1}, a_{12} can be obtained by:

$$a_{12} = h_{M1} + \frac{h_{TEP}-h_{M1}}{2}. \quad (21)$$

It is assumed that the change rate of dynamic pressure is zero at the altitude of h_{TEP}, i.e., $\frac{d\bar{q}}{dh}(h_{TEP}) = 0$, and $\bar{q}(h_{M1}) = \bar{q}_C$. Then, solving the first equation of Eq. (20) gives:

$$a_{11} = \frac{\bar{q}_C - \bar{q}_{TEP}}{\frac{(h_{M1}-a_{12})^3 - (h_{TEP}-a_{12})^3}{3} - (h_{M1}-h_{TEP})(h_{TEP}-a_{12})^2}, \quad (22)$$

$$a_{13} = -a_{11}(h_{TEP}-a_{12})^2. \quad (23)$$

Applying the similar treatment to a_{21}, a_{22}, and a_{23} achieves:

$$\begin{aligned} a_{22} &= h_{ALI} + \frac{h_{M2}-h_{ALI}}{2} \\ a_{21} &= \frac{\bar{q}_{ALI} - \bar{q}_C}{\frac{(h_{ALI}-a_{22})^3 - (h_{M2}-a_{22})^3}{3} - (h_{ALI}-h_{M2})(h_{M2}-a_{22})^2}. \\ a_{23} &= -a_{21}(h_{M2}-a_{22})^2 \end{aligned} \quad (24)$$

Remark 3. The overall $\frac{d\bar{q}}{dh}$ profile is always comprised of two quadratic segments and a zero segment, as shown in Fig. 2. A smooth dynamic pressure profile is induced with a constant dynamic pressure profile $\bar{q}_C$ in the middle phase. As the range of $\bar{q}_C$ in the middle phase (denoted by $[h_{M2}, h_{M1}]$) decreases, its change rate on two polynomial phases will reduce, as can be observed from dashed line of Fig. 2.

Remark 4. It is worth noting that this strategy is different from the US space shuttle TAEM strategy [10] for holding a constant γ ($\bar{q}$ is meandering) where the flight performance gives way to smaller N_z for crews' riding comfort. However, the unmanned RLV does not have to comply with this constraint. Thus, the constant dynamic pressure profile is developed as the reference one in the middle phase. Moreover, in comparison of the Mach number profile developed in [16] and dynamic pressure profile used in [27], the longitudinal profile proposed above shows a more explicit physical meaning.

Given the reference profiles of dynamic pressure with respect to the altitude, a TAEM trajectory iteration algorithm is developed, as shown in Fig. 3. The flow chart indicates that state variables are iterated to balance RLV dynamic equations using two nested loops at each node of altitude.

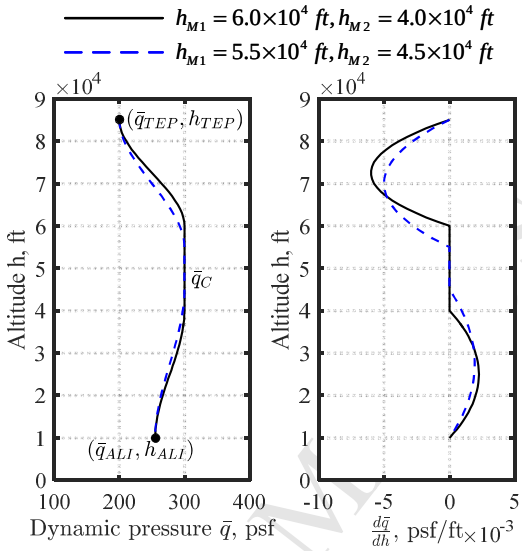

Fig. 2: Diagram of dynamic pressure profiles and its change rate with respect to altitude

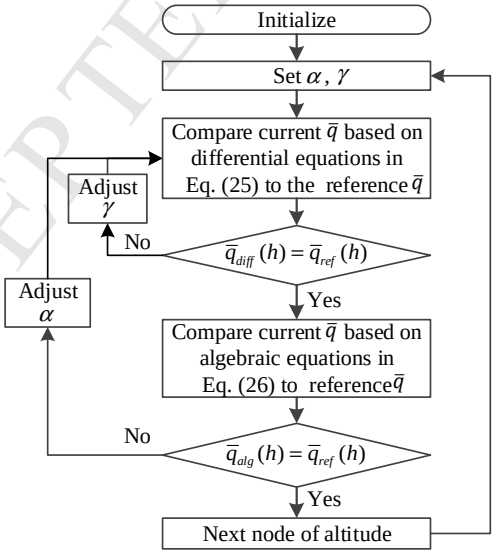

Fig. 3: TAEM trajectory iteration algorithm

Firstly, the flight-path angle is adjusted in the inner loop to ensure that the dynamic pressure in Eq. (25) equals to the reference one defined in Eq. (20) via secant iteration method.

$$\bar{q}_{diff}(h) = \bar{q}_{TEP} + \frac{d\bar{q}}{dh}\, dh, \tag{25}$$

where $\frac{d\bar{q}}{dh}$ is defined in Eq. (11).

Subsequently, the angle of attack is regulated to balance another estimation of dynamic pressure (see Eq. (26)) rearranged from Eq. (13) to the reference one in Eq. (20).

$$\bar{q}_{alg}(h) = \frac{mgcos\gamma}{S_{ref}C_L cos\mu - \frac{2msin\gamma}{\rho}\frac{d\gamma}{dh}} \tag{19}$$

By the above propagation, trajectory parameters $\bar{q}_i$, γ_i, and α_i are obtained at each altitude node h_i. The corresponding range-to-go R_i at each altitude node is then calculated by integrating Eq. (15) from the current node to the end node:

$$R_i = \sum_{j=i}^{n-1} \frac{h_{j+1}-h_j}{\tan\gamma_{j+1}} \tag{27}$$

where $i = 1,2,\cdots,n$ denotes the number of altitude node. Note that if enough altitude node is set, the rang-to-go can be obtained with good precision.

The whole trajectory histories in terms of $\bar{q}$, γ, α, and h with respect to R are obtained. Meanwhile, the history of normal acceleration N_z, as an important guidance command, is obtained based on Eq. (28).

$$N_z = \frac{Lcos\alpha + Dsin\alpha}{mg} + sin\gamma sin\alpha - cos\gamma cos\alpha cos\mu \tag{28}$$

Finally, all the reference signals at each node are recorded and coded in the guidance scheme as a lookup table. Note that in this section only the vertical motion is considered, hence the terms containing the bank angle in Eq. (26) is removed by assuming $cos\ \mu = 1$.

The trajectory iteration algorithm in Fig. 3 can ensure that the altitude and dynamic pressure satisfy with the desired ones. The next step is to adjust the ground-track path on the purpose of guiding the RLV to the desired position. To this end, in Section 4, an onboard ground-track predictor is constructed to generate the signal of range-to-go, which is used as an index to select the longitudinal reference command. In addition, the lateral reference command is generated as well. This results in the connection between the longitudinal and lateral motions.

4. Onboard Ground-Track Predictor

In this paper, the ground-track path is essentially composed of three distinct parts, as shown in Fig. 4. It starts from TEP followed by acquisition (AC) phase, where the RLV turns to align its heading with a tangency point on the HAC. After a flight phase of straight-line ground-track, the RLV banks and turns to fly the HAC. It is worth

noting that the RLV can choose either direct HAC mode or overhead HAC mode according to its flight ability. At last, the pre-final landing (PFL) phase is initiated, where the position and heading are modified further to align the RLV to the runway by the guidance system.

Based on the constructed ground-track path, the onboard ground-track predictor is then designed to provide two critical features. 1) At the terminal entry point, the total range-to-go R_{total} of the vehicle is predicted which is used as an index to choose the right trajectory to follow. 2) During the TAEM flight, the range-to-go R_{tg} at each point on the flight path is predicted in real-time, according to which reference commands are then generated by the lookup table.

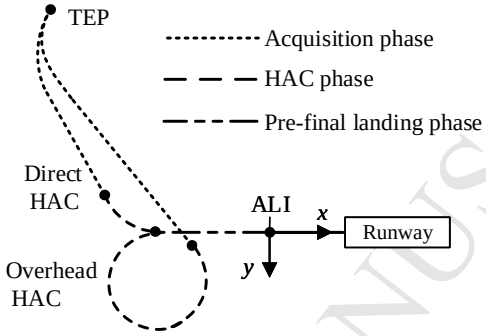

Fig. 4: Ground-track path for the TAEM flight

Using the reverse derivation and working backwards along the trajectory, the working principle of GTP is described below. Firstly, during the PFL phase, the GTP regards the length along the runway as the range to go. In this process, the error of cross-range from runway centerline is neglected for simplification, since the range along the runway is much larger than the cross range. Thus, the prediction of range-to-go for PFL phase (red line in Fig. 5), defined as S_{PFL}, is calculated by:

$$S_{\mathrm{PFL}} = \sqrt{x + y^2}, \tag{29}$$

where (x, y) denotes the current position of the RLV.

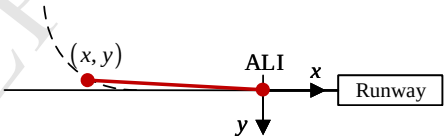

Fig. 5: Ground-track prediction for pre-final landing phase

During the phase of HAC, the GTP is required to predict the range around HAC and PFL range, as can be observed from red line of Fig. 6. Defining the radius of HAC as R_{HAC} and assuming that the center of HAC locates at (X_{HAC}, Y_{HAC}), the predicted range-to-go S_{HAC} can then be obtained by:

$$S_{HAC} = R_{HAC}\Delta\psi + |X_{HAC}|, \tag{30}$$

where $\Delta\psi$ is the heading angle to go. If taking both the overhead and direct HAC turning mode into consideration, $\Delta\psi$ is given by a two-sectioned equation as:

$$\Delta\psi = \begin{cases} arccos\left(sgn(Y_{HAC})\frac{Y_{HAC}-y}{\sqrt{(X_{HAC}-x)^2+(Y_{HAC}-y)^2}}\right), x < X_{HAC} \\ 2\pi - arccos\left(sgn(Y_{HAC})\frac{Y_{HAC}-y}{\sqrt{(X_{HAC}-x)^2+(Y_{HAC}-y)^2}}\right), x \geq X_{HAC} \end{cases}, \quad (31)$$

with $sgn(Y_{HAC})$ denoting the sign of Y_{HAC}.

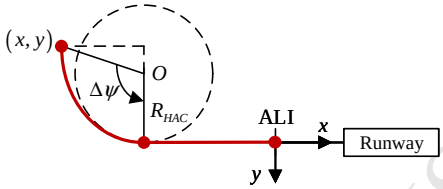

Fig. 6: Ground-track prediction for the HAC phase

During the AC phase, as indicated by the red line of Fig. 7, the GTP calculates partial AC range and total range of

HAC and PFL phase denoting by S_{PRED2}. Thus, the predicted range-to-go at AC phase is calculated by:

$$S_{AC} = R_{TAC}|\Delta\psi_{AC}| + S_{SL} + S_{PRED2}, \quad (32)$$

where the arc range at the initial phase of acquisition is approximately calculated by multiplying the radius of the arc R_{TAC} with $|\Delta\psi_{AC}$, the intersection angle between the current heading and the tangent line of HAC. The value of R_{TAC} is obtained by exploiting the principle of coordination turning:

$$R_{TAC} = \frac{V^2 cos\gamma}{g tan\mu_{avr}}, \quad (33)$$

with μ_{avr} denoting the average bank angle determined by the Mach number. In addition, S_{SL} is the straight-flight range during the AC phase. Regarding its computation, two straight-line distances S_A and S_B are involved, as illustrated in Fig. 7. Defining R_{TAN} as the straight-line distance between point *A* (the current position of RLV) and point *O* (the center of HAC), the calculations of S_A and S_B can be described by:

$$S_A = R_{TAC}(1 - cos(|\Delta\psi_{AC}|)), \quad (34)$$

$$S_B = R_{TAN} - R_{TAC} sin(|\Delta\psi_{AC}|). \quad (35)$$

The straight-flight range during the AC phase is then obtained by $S_{SL} = \sqrt{{S_A}^2 + {S_B}^2}$.

Furthermore, as shown in Fig. 8, the heading angle command ψ^* for AC phase is achieved by:

$$\Delta\psi = \psi_1 - \psi_2, \quad (36)$$

where $\psi_1 = \angle AOB$ can be calculated using the same principle depicted in Eq. (31), and ψ_2 can be achieved by:

$$\psi_2 = arccos\left(\frac{R_{HAC}}{\sqrt{(X_{HAC}-x)^2+(Y_{HAC}-y)^2}}\right). \tag{37}$$

Then, R_{TAN} in Eq. (35) can be obtained by:

$$R_{TAN} = R_{HAC}tan\psi_2. \tag{38}$$

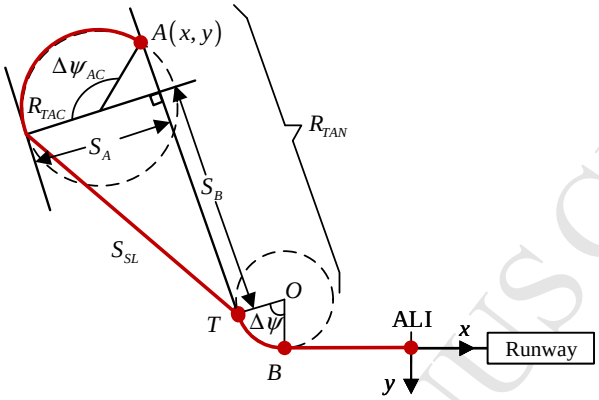

Fig. 7: Ground-track prediction for the AC phase

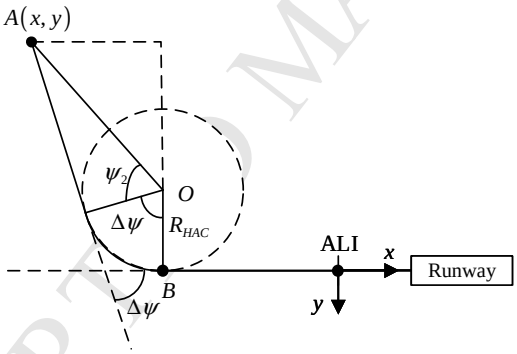

Fig. 8: Heading angle command for the AC phase

Through the above propagation, the range-to-go R_{tg} at each point on the flight path can be predicted by the GTP in real-time. By lookup table, corresponding reference longitudinal commands can be obtained. Meanwhile, the GTP also generates the reference command of heading angle, by tracking which the vehicle trajectory can be adjusted to align to the runway.

Remark 5. In this study, since the HAC radius and the ALI location are fixed, the ground-track path generated by GTP is fixed. Then the longitudinal commands are generated in real-time by lookup table where GTP range-to-go R_{tg} is regarded as an index. The constant HAC radius rather than cylindrical HAC is used for the sake of the computational efficiency of the onboard ground-track predictor.

Remark 6. As can be observed from Fig. 4, the RLV is expected to fly with a small arc at the beginning of TAEM, followed by a wide range of straight-line, rather than to keep a sustained turning with a large bank angle during a supersonic flight [18]. By virtue of the proposed strategy, the banking capability of a RLV can be relaxed for abnormal conditions, and turning maneuver can be achieved more easily since the alignment to runway is completed primarily by HAC phase with a subsonic flight.

5. Onboard Guidance Law Design

5.1. Longitudinal Commands from Guidance Scheme

The objective of longitudinal guidance is to track the reference profile in terms of the altitude and the velocity. The normal acceleration N_z and speedbrake δ_{sb} are two guidance states for the longitudinal profile tracking. The total normal acceleration command N_{zc} consists of reference command $N_z{}^*$ and closed-loop term ΔN_z:

$$N_{zc} = N_z{}^* + \Delta N_z, \tag{39}$$

where N_z^* is adopted directly from the longitudinal trajectory generation module (see Section 3), and a proportional derivative scheme is used for the closed-loop term:

$$\Delta N_z = K_H(h^* - h) + K_{HI}\int(h^* - h) + K_{HD}\left(\dot{h}^* - \dot{h}\right). \tag{40}$$

Note that a single set of gains are not appropriate in response to a wide range of altitude tracking. Nine sets of control gains are firstly determined for specific altitude points at the design stage. Interpolation lookup method can then be used to obtain gains at other intermediate altitude points in simulation verification.

As far as the velocity tracking task is concerned, the speedbrake is initiated as an actuator when $M \leq 0{:}8$. The proportional-integral law is employed:

$$\delta_{sbc} = K_V(V^* - V) + K_{VI}\int(V^* - V). \tag{41}$$

Remark 7. It is worth emphasizing that the normal acceleration N_z instead of the angle of attack α servers as a guidance state in this paper. This is due to the fact that, on one hand, the precision deterioration of measuring angle of attack is usually induced in a high speed; on the other hand, the RLV is always subject to the mechanical constraint (namely the load factors) which can be featured by the normal acceleration. Thus the normal acceleration is selected as a control signal.

The normal acceleration command cannot be immediately introduced in the dynamic model (Eqs. (1)-(6)), since it is not a valid input signal of the dynamic equations. It has to be transformed into the form of angle of attack. To this end, the approximated expression between the normal acceleration and the angle of attack is derived.

Firstly, recall the definition of normal acceleration under body-axis system in Eq. (28). By assuming that $\alpha = \mu = 0$, and using Eq. (2), one can render:

$$N_z \approx \frac{L - mg\cos\gamma}{mg} = \frac{V}{g}\dot{\gamma}. \tag{42}$$

Given that steady flight state is achieved for a RLV, $q = \dot{\theta} \approx \dot{\gamma}$. Hence, the commanded pitch rate q_c can be rendered as:

$$q_c = \frac{gN_{zc}}{V}. \tag{43}$$

It is evident that the command of normal acceleration is replaced by pitch rate through Eq. (43). The next step for the guidance system verification is to transform the command of q to that of α. By recalling the mathematical relationship between α, θ and γ:

$$\dot{\alpha} = \dot{\theta} - \dot{\gamma} = q - \dot{\gamma}, \tag{44}$$

and using Eq. (2) without consideration given to the effect of lateral motion, one can obtain:

$$\dot{\alpha} = q - \frac{\bar{q}S_{ref}C_{L\alpha}}{mV}\alpha, \tag{45}$$

where $C_{L\alpha}$ denotes the angle of attack dependent lift coefficient term. Furthermore, by applying Laplace transformation to Eq. (45), the relational expression between angle of attack and pitch rate is approximately constructed in Laplace domain as:

$$\alpha = \frac{T_i}{T_i s+1} q, \tag{46}$$

with $T_i = \frac{mV}{\bar{q}S_{ref}C_{L\alpha}}$.

As a consequence, the commanded angle of attack α_c can be conceived by integrating the open-loop term α^* and the close-loop term derived from N_z using Eqs. (43) and (46):

$$\alpha_c = \alpha^* + \frac{T_i}{T_i s+1}\frac{gN_{zc}}{V}, \tag{47}$$

Remark 8. The above procedure is merely executed for the guidance scheme verification at first stage of G&C design. In fact, during the follow-up design process, where integrated G&C is considered and 6-DOF dynamic model is used, it is the pitch rate command in Eq. (43) that is directly inserted into the flight control module. However, this is beyond the current topic.

5.2. Bank Angle Command from Guidance Scheme

The lateral guidance law calculates the commanded bank angle, such that the ground-track path depicted in Section 4 can be followed. As a consequence of the split flight phases, the bank angle command is separated for each phase.

For the AC phase, the bank angle is proportional to the heading deviation from the tangent to the HAC:

$$\mu_c = K_\psi(\psi - \psi^*), \tag{48}$$

where ψ^* denotes reference heading angle adopted from Eq. (36), and ψ is the actual heading angle.

For the HAC phase, the bank angle command is a sum of the reference term μ^* and the close-loop term $\Delta\mu$:

$$\mu_c = \mu^* + \Delta\mu, \tag{49}$$

where μ^* is the required bank angle for turning with a specific HAC radius, and it can be derived from Eq. (33):

$$\mu^* = \arctan\left(\frac{V^2 cos\gamma}{gR_{\mathrm{HAC}}}\right). \tag{50}$$

The deviation signal $\Delta\mu$ is obtained by taking a proportional-derivative law for ΔR, i.e., the deviation between the real radius of HAC and the reference one:

$$\Delta\mu = K_Y \Delta R + K_{YD} \Delta\dot{R}. \tag{51}$$

During the PFL phase, a classical proportional-differential (PD) scheme is exploited for correcting further the cross-track range. Thus, the bank angle command is generated by combining the lateral deviation and its derivative from the extension of the runway centerline:

$$\mu_c = K_{Y2} \Delta y + K_{YD2} \Delta\dot{y} \tag{52}$$

6. Numerical Simulations and Analysis

The simulations of the proposed TAEM guidance system are performed based on the model of X-34 vehicle [28]. The main features of the X-34 vehicle are given in Table 2. Instead of the traditional standard drag polar model, the piecewise polynomial model [25] is used to describe the RLV aerodynamics during the TAEM phase:

$$C_L = \begin{cases} C_{l01} + C_{l11}\alpha + C_{l21}\alpha^2, M_1 = 0.3 \\ C_{l02} + C_{l12}\alpha + C_{l22}\alpha^2, M_2 = 0.4 \\ \vdots \\ C_{l0p} + C_{l1p}\alpha + C_{l2p}\alpha^2, M_p = 3.0 \end{cases} \tag{53}$$

$$C_D = \begin{cases} C_{d01} + C_{d11}\alpha + C_{d21}\alpha^2 + C_{d31}\alpha^3 + C_{s11}\delta_{sb}, M_1 = 0.3 \\ C_{d02} + C_{d12}\alpha + C_{d22}\alpha^2 + C_{d32}\alpha^3 + C_{s12}\delta_{sb}, M_2 = 0.4 \\ \vdots \\ C_{d0p} + C_{d1p}\alpha + C_{d2p}\alpha^2 + C_{d3p}\alpha^3 + C_{s1p}\delta_{sb}, M_p = 3.0 \end{cases} \tag{54}$$

where $M_j (j = 1, \cdots, p)$ is the jth Mach number within the range of $[0.5, 3.0]$, $C_{lij} (i = 0,1,2)$ is the coefficient of degree i for C_L at Mach number M_j, $C_{dij} (i = 0,1,2,3)$ is the coefficient of degree i for C_D at Mach number M_j, and C_{s1j} describes the speedbrake's contribution to drag at Mach number M_j. Note that $C_{s1j} = 0$ if $M_j > 0.8$. C_L and C_D at intermediate Mach numbers are evaluated by finding a weighted average of the polynomial fits at the two nearest Mach numbers.

In the following simulation studies, the longitudinal profiles are firstly given. Then two simulation cases are conducted using the platform as shown in Fig. 1 to validate the effectiveness of the proposed TAEM guidance system.

The first case considers variations in initial position and heading angle, whilst vehicle model uncertainties are involved

in second case. Regarding altitude tracking law Eq. (40), lookup table is applied to determine the control gains as

shown in Table 3. Fixed control gains are designed for velocity tracking law Eq. (41) and lateral guidance law Eqs. (48), (51) and (52) as: $K_V = 0.015$, $K_{VI} = 0.03$, $K_\psi = 1.5$, $K_Y = 0.007$, $K_{YD} = 0.008$, $K_{Y2} = 0.005$, and $K_{YD2} = 0.007$.

Table 2: The main features of X-34 vehicle

Feature	Value
Mass, $slug$	560
Wing chord, ft	14.5
Wing span, ft	27.7
Reference area, ft^2	357.5
Max L/D ratio	between 2 and 8

Table 3: The control gains at different altitude points

$h, 10^4 ft$	1	2	3	4	5	6	7	8	8.5
$K_H, 10^{-3}$	3.0	2.4	1.4	1.2	0.9	0.7	0.6	0.5	0.4
$K_{HI}, 10^{-4}$	3.0	2.6	2.4	2.0	1.0	1.0	1.0	1.0	1.0
$K_{HD}, 10^{-3}$	1.5	1.5	1.3	1.3	0.9	0.8	0.7	0.6	0.5

6.1. Longitudinal Profiles Generation

The TAEM phase starts from the altitude of $h_{TEP} = 85{,}000ft$ with dynamic pressure of $\bar{q}_{TEP} = 200psf$ (i.e., $V_{TEP} = 2456\ ft/s$). The terminal altitude and the terminal dynamic pressure are set as $h_{ALI} = 10{,}000\ ft$ and $\bar{q}_{ALI} = 255\ psf$, respectively. The altitude range for constant reference $\bar{q}$ profile in Eq. (20) are selected as $h_{M2} = 45{,}000ft$, and $h_{M1} = 55{,}000ft$, respectively. A short period of constant $\bar{q}$ segment is designed to give way to the small change rate of dynamic pressure at two polynomials segments.

It is exhibited in Fig. 9 that the dynamic pressure varies smoothly from TEP to ALI. A change rate of zero is achieved at both TEP and ALI points for QEG flights. The dynamic pressure is set to be bounded by $[\bar{q}_{\min}, \bar{q}_{\max}] = [110, 400]psf$ at the middle stage of TAEM, ensuring that it is between the pressure of maximum dive and maximum glide that the RLV can perform. Fig. 10 shows the profiles of energy height with respect to range-to-go, i.e., the energy corridor. All the energy height profiles are bounded by the max dive profile (represented by the dashed line in Fig. 10) and max glide profile (shown by the dot-dashed line in Fig. 10). Fig. 11 illustrates the history of the altitude (Fig. 11(a)), the velocity (Fig. 11(b)), the angle of attack (Fig. 11(c)), and the normal acceleration (Fig.

11(d)) with respect to the range-to-go. These trajectory commands are regarded as open-loop commands in the proposed guidance scheme. It is worth noting that different $\bar{q}$ versus h profiles means different gliding range a RLV can perform. For the studied X-34 vehicle, the gliding range is within $[R_{\min}, R_{\max}] = [3.835, 6.533]10^5\, ft$, as shown in Fig. 11(a). But the feasible range might be smaller than this domain when considering the error tolerant capability of the guidance scheme.

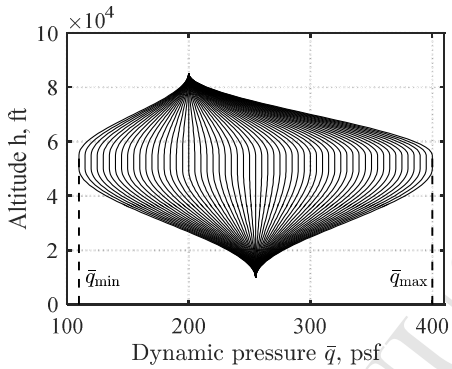

Fig. 9: Different profiles of dynamic pressure versus altitude

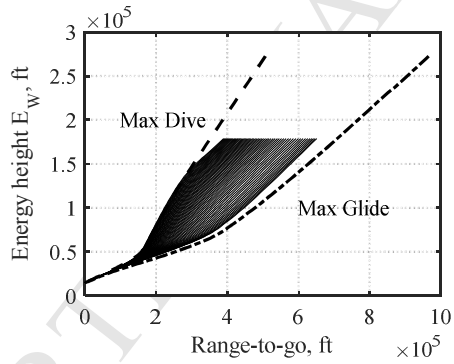

Fig. 10: Profiles of energy height versus range-to-go for different dynamic pressure

6.2. Trials with Initial Position and Heading Variations

To verify the feasibility of the proposed guidance strategy for TAEM flight in the presence of large initial condition variations, several tests are carried out. In all these tests, the initial value of dynamic pressure is fixed at $\bar{q}_{TEP} = 200psf$ (i.e., $M = 2.5$), and the initial altitude is fixed at $h_{TEP} = 85,000ft$. The initial states subject to variations are listed in Table 4, including cross-tack position x_0, down-track position y_0, and heading angle ψ_0.

Fig. 12 presents the ground-track paths for eight different initial entry points which are marked in blue stars. Since both of two turning modes (direct HAC and overhead HAC) are considered, sixteen paths are obtained in total. The results of the first four cases are stated in Table 4, and the other four cases are omitted since they are symmetrical to the first four cases with *x*-axis. In these cases, the RLV starts from different initial positions with various heading angles, but ends at almost the same terminal position with nearly zero heading angle. Table 4

reveals that, for all the first four cases, the final downrange errors $|\Delta x|$ are less than 100 *ft*, the final cross-range errors $|\Delta y|$ are nearly zero, and the final altitude errors $|\Delta h|$ are less than 100 *ft*.

Moreover, the profiles of energy height with respect to range-to-go are depicted in Fig. 13, for the first four cases with different turning modes. It can be observed that initial and terminal energies of the RLV in all cases are the same.

But different ground-track paths are achieved as shown in Fig. 12. This is due to the fact that different range-to-go is predicted by the onboard ground-track predictor developed in Section 4, when the RLV suffers from changes in initial positions and heading angles. While the terminal constrains are satisfied benefiting from the trajectory generation algorithm constructed in Section 3.

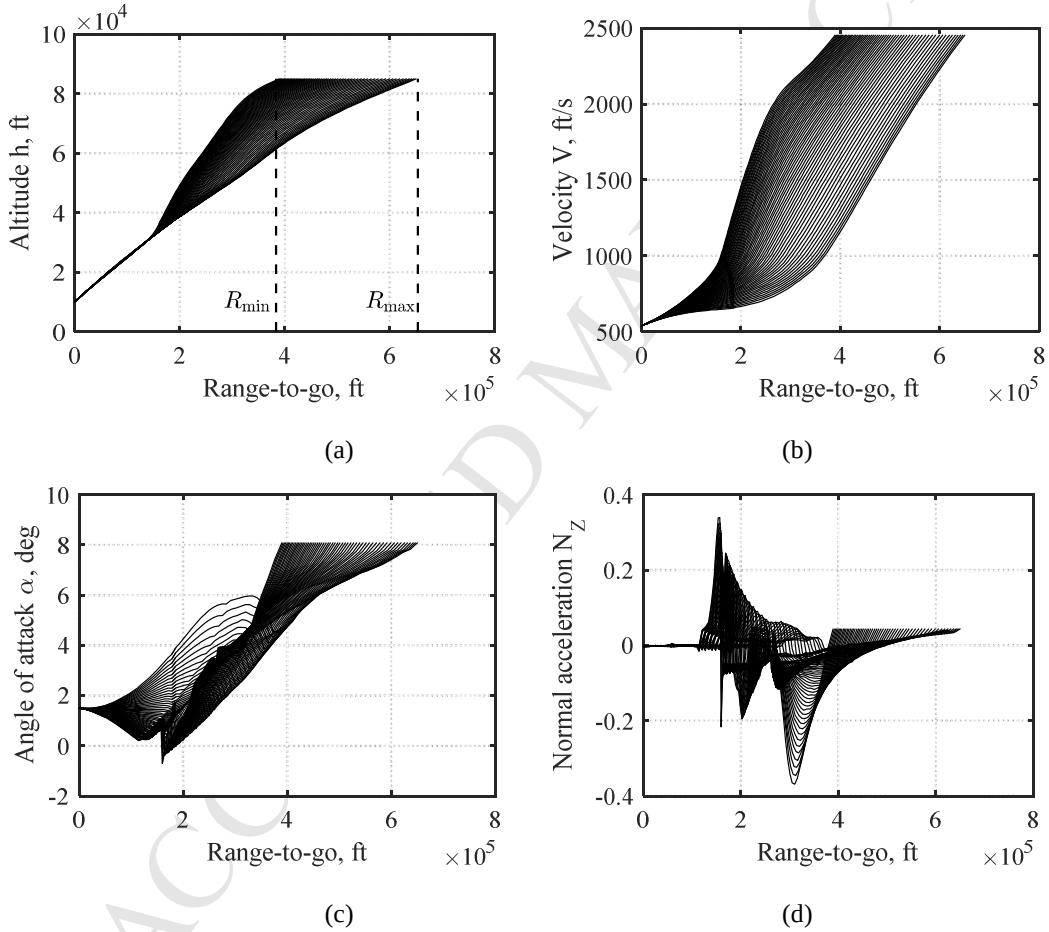

Fig. 11: The states histories versus range-to-go for different dynamic pressure

The profiles of dynamic pressure with respect to range-to-go are illustrated in Fig. 14 for different simulation cases. Due to the consideration of coupling between longitudinal and lateral motion, the dynamic pressure profiles show a slight difference compared with the reference ones where the constant dynamic pressure is designed in the middle phase, as described in Section 3. The corresponding altitude and velocity histories with respect to range-to-

go are depicted in Fig. 15. For all cases, the RLV ends at ALI points with altitude of around 10; 000 *ft* and velocity of around 539.2 *ft/s* (i.e, *M* = 0.5) as expected. Moreover, Fig. 15(a) shows that the gliding range for these cases is within $[\tilde{R}_{min}, \tilde{R}_{max}] = [4.394, 5.951]10^5\, ft$.

In general, the satisfactory performance achieved in these test cases demonstrates the adaptation capability of the proposed TAEM guidance scheme in the presence of variations in initial position and heading angle.

Table 4: TAEM guidance with different initial conditions

Case	x_0, ft	y_0, ft	ψ_0, deg	TM	x_f, ft	y_f, ft	h_f, ft
1	-3×10^5	-3×10^5	60	1	-93.73	-0.014	9908.5
				2	-66.72	0.012	9987.1
2	-2×10^5	-4×10^5	45	1	-13.67	-0.013	9895.3
				2	-8.08	0.011	10005
3	1×10^5	-4×10^5	90	1	-66.7	0.013	9911.4
				2	7.25	0.012	9977.4
4	2.5×10^5	-2.5×10^54	135	1	-52.38	-0.013	9901.8
				2	-33.58	0.012	9930.9

Target states at touchdown: $x_f = y_f = 0\, ft, h_f = 10,000\, ft$.

TM: Turning Mode, 1: Direct HAC, 2: Overhead HAC.

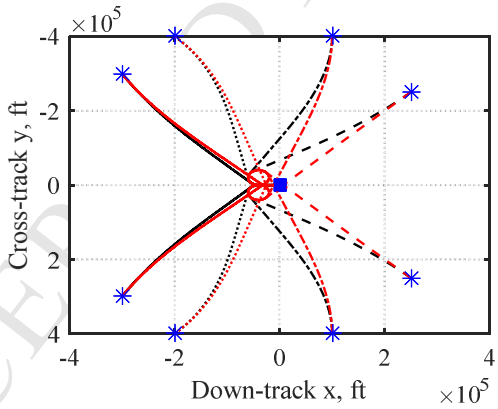

Fig. 12: Ground-track paths with different initial positions and heading angles

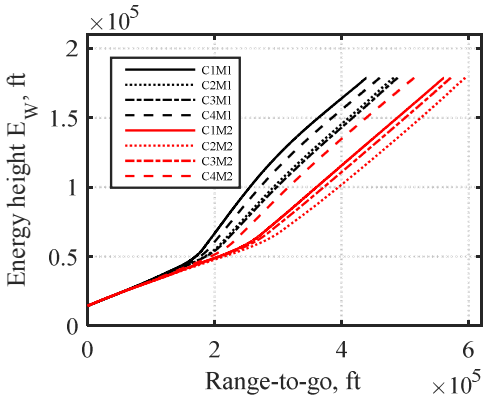

Fig. 13: Energy height profiles with different initial positions and heading angles

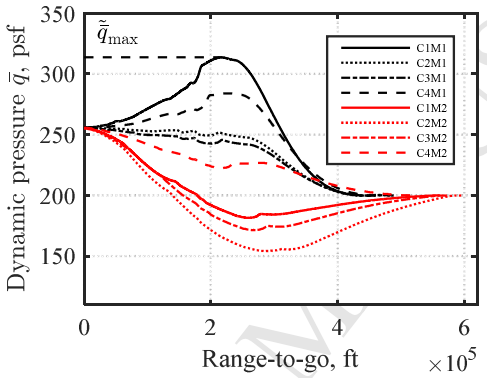

Fig. 14: Dynamic pressure profiles with different initial positions and heading angles

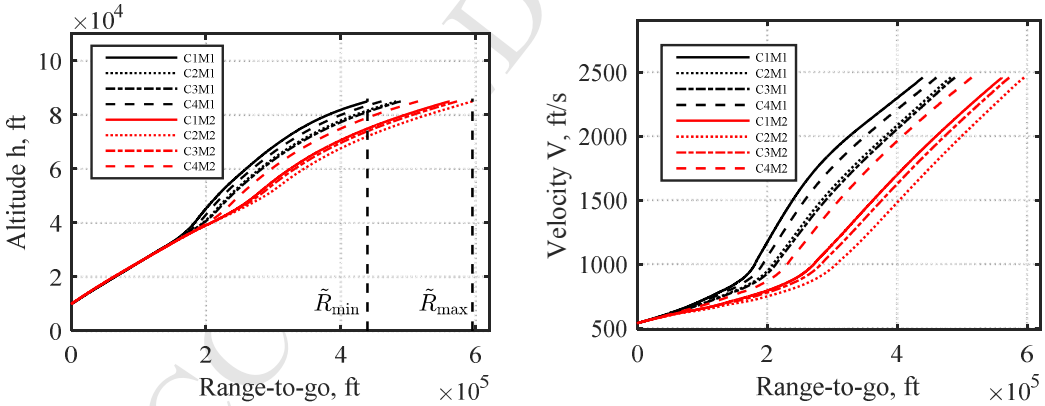

Fig. 15: Altitude and velocity profiles with different initial positions and heading angles

6.3. Trials with Model Uncertainties

In this subsection, the robustness of the proposed guidance system is validated by injecting model uncertainties into the RLV model. Taking Case 1 with turning mode 1 in the above subsection as a nominal case, thirty tests with perturbations are carried out. The aerodynamic lift coefficients C_L, the aerodynamic drag coefficients C_D, the

atmospheric density ρ, and vehicle mass m are subject to the uniform random perturbation in the range of [-10%, 10%], as studied in [20].

Fig. 16 shows the ground-track paths and altitude profiles for all the thirty cases. It is indicated that the proposed guidance scheme performs nearly the same trajectories and successfully drives the RLV to the desired terminal point. The corresponding histories of the flight-path angle and Mach number are depicted in Fig. 17. The commands generated by the proposed TAEM guidance scheme, including the speedbrake, the angle of attack, and the bank angle are presented in Fig. 18. From Fig. 18(a), the speedbrake is initiated when $M \leq 0{:}8$ in order to dissipate the energy.

Moreover, Monte-Carlo simulation tests with 300 runs are conducted to further validate the robustness and precision of the proposed guidance scheme. In each case, the simulation is terminated when the RLV reaches the altitude of $10{,}000ft$.

The final guidance performance can be observed from Fig. 19. The maximum final errors of down-track position and cross-track position are less than $100ft$ and $0.1ft$, as shown in Fig. 19(a) and Fig. 19(b), respectively. As compared to the traditional method in [10] where the terminal constraints are $|\triangle x_f|$ of $100ft$ and $|\triangle y_f|$ of $300ft$, the proposed approach achieves sufficient precision on final position for TAEM guidance. The final error distributions for the flight-path angle and heading angle are presented in Fig. 19(c) and Fig. 19(d), respectively. It is evident that the flight-path angle and heading angle meet the predefined constraints very well. The final error of dynamic pressure is shown in Fig. 19(e) with a max error less than $40psf$, which is acceptable as stated in [19]. The big dynamic pressure error exhibits mainly due to that the speedbrake only initiates at finial subsonic stage of the TAEM flight, which makes it difficult to compensate large deviations arising from supersonic and transonic flight. Nonetheless, the corresponding Mach number shows a small difference from the desired Mach 0.5, as shown in Fig. 19(f).

In addition, the maximum and minimum values of dynamic pressure during the TAEM flight are illustrated by green and blue marker in Fig. 20(a), respectively. The normal acceleration's range during the flight is displayed in Fig. 20(b). It is shown that the constraints on dynamic pressure and normal acceleration, as listed in Table 1, are well satisfied.

Note that, the nominal reference dynamic pressure for these cases is about $\tilde{\bar{q}}_{max} = 314psf$ as can be observed from solid black line in Fig. 14. However, in the presence of system uncertainties, Fig. 20(a) shows that the maximum dynamic pressure in-flight is almost $400psf$. This implies that the achievable gliding range of the proposed guidance scheme is less than the ideal range ($[R_{min}, R_{max}]$ as shown in Fig. 11(a)), when considering robustness to system uncertainties. Instead, it is indicated that the initial range deviations within $[\tilde{R}_{min}, \tilde{R}_{max}]$ (see Fig. 15(a)) can be effectively handled, in the case involving 10% uncertainties on aerodynamic, environment, and vehicle mass.

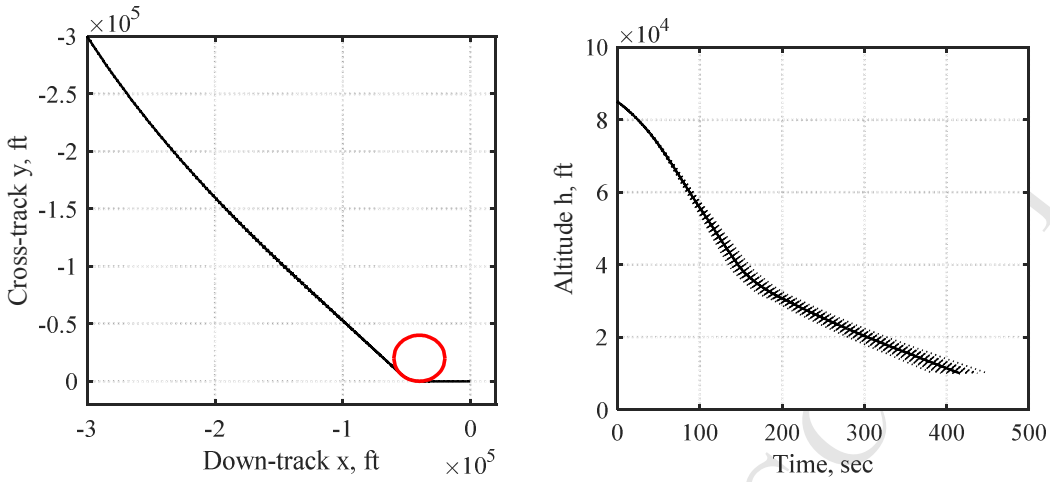

(a) (b)

Fig. 16: The trajectories with model uncertainties

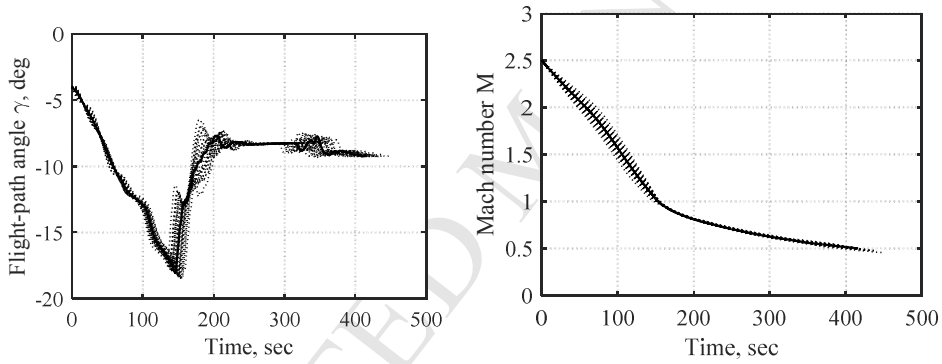

(a) (b)

Fig. 17: The flight-path angle and Mach number profiles with model uncertainties

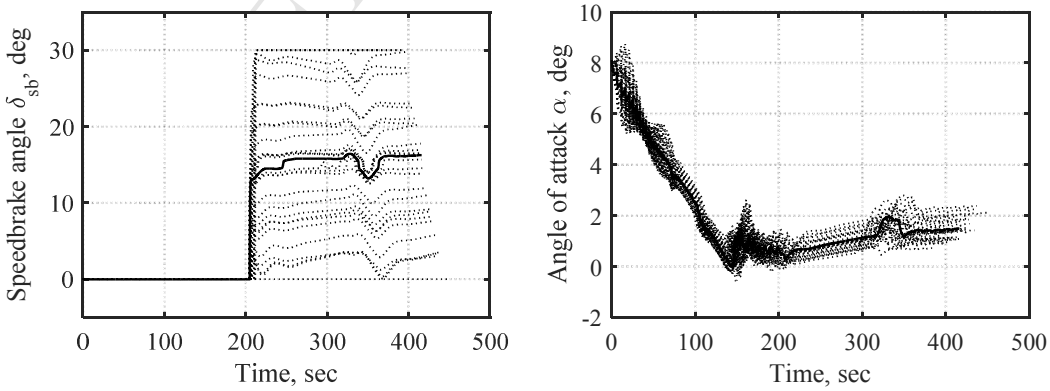

(a) (b)

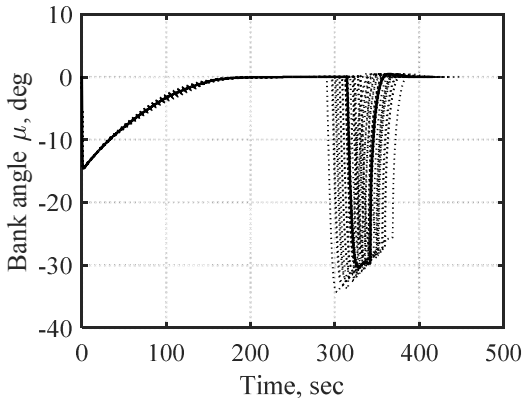

(c)

Fig. 18: The commands generated by the proposed guidance system

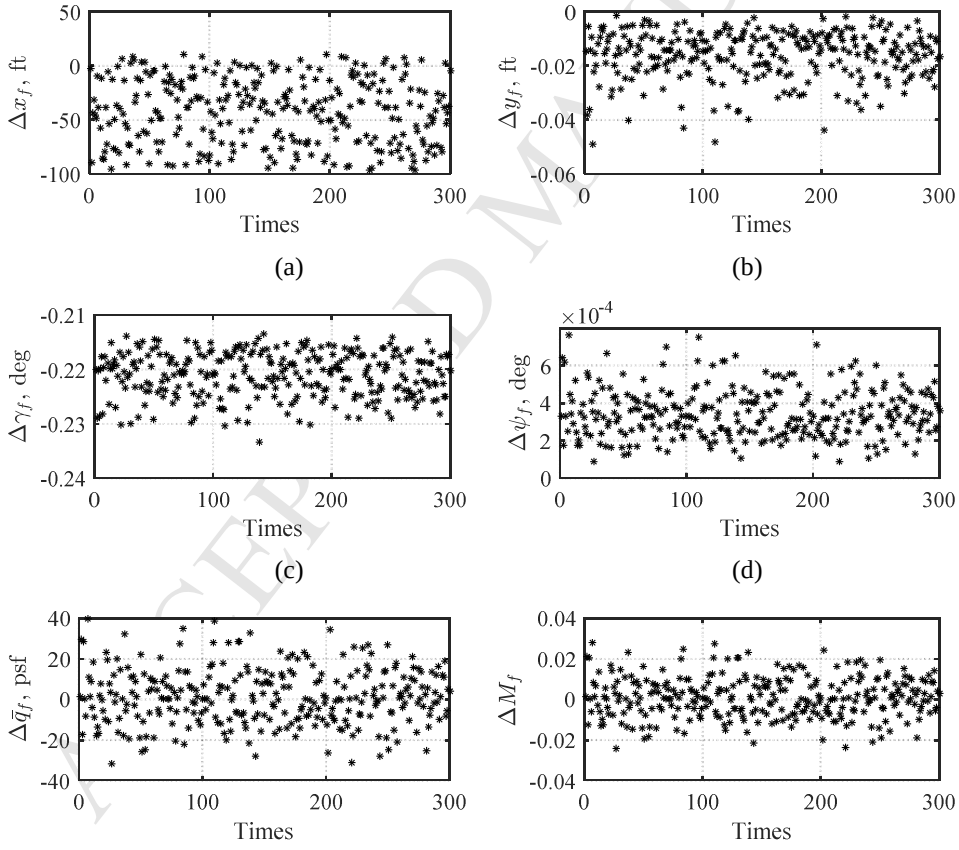

(a) (b) (c) (d) (e) (f)

Fig. 19: Final error distribution for Monte Carlo test

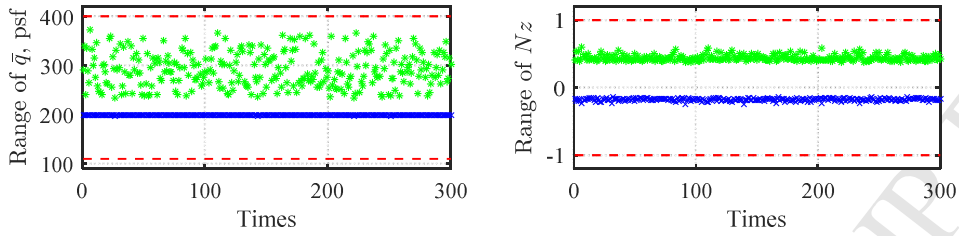

(a) (b)

Fig. 20: Constraints during the TAEM flight

7. Conclusions

In this paper, an onboard guidance scheme is proposed for an unpowered RLV during the TAEM phase flight. The longitudinal strategy is specified by a reference dynamic pressure profile. This longitudinal profile is pre-designed based on the analysis of a RLV's flight ability. While, in the presence of variations in initial position and heading angle, the onboard ground-track predictor is operating to make sure that the RLV can be guided to the desired terminal position. For trajectory tracking, the guidance law is designed, where the normal acceleration rather than angle of attack is regarded as a longitudinal guidance command with consideration of realistic flight situations. In simulation tests, not only changes in the initial conditions, but also uncertainties on system model, are investigated. The results demonstrate that the proposed guidance scheme can achieve satisfactory performance, even under off-nominal conditions.

However, to improve the capability to tolerant larger range error at the terminal entry point, the ground-track path with a fixed radius of heading alignment cylinder could be relaxed by changing the radius of heading alignment cylinder. On the other hand, instead of the simple guidance law, more advanced guidance algorithms with robustness to larger uncertainties on system model are needed.

Acknowledgments

The authors would like to thank the Editors and the anonymous reviewers whose insightful comments have helped

to improve the quality of this paper considerably. The authors would also like to acknowledge the financial supports from National Natural Science Foundation of China (under Grants 61573282 and 61603130) and Natural Sciences and Engineering Research Council of Canada (NSERC) for the work reported in this paper.

References

[1] D. C. Freeman, T. A. Talay, R. E. Austin, Reusable launch vehicle technology program, Acta Astronautica 41 (11) (1997) 777–790.

[2] C. Tomatis, L. Bouaziz, T. Franck, J. Kauffmann, RLV candidates for european future launchers preparatory programme, Acta Astronautica 65 (1) (2009) 40–46.

[3] J. Hanson, A plan for advanced guidance and control technology for 2nd generation reusable launch vehicles, in: AIAA Guidance, Navigation, and Control Conference and Exhibit, 2002, pp. 4557–4577.

[4] H. Yan, S. Tan, Y. He, A small-gain method for integrated guidance and control in terminal phase of reentry, Acta Astronautica 132 (2017) 282–292.

[5] B. L. Tian, W. R. Fan, R. Su, Q. Zong, Real-time trajectory and attitude coordination control for reusable launch vehicle in reentry phase, IEEE Transactions on Industrial Electronics 62 (3) (2015) 1639–1650.

[6] C. A. Kluever, D. A. Neal, Approach and landing range guidance for an unpowered reusable launch vehicle, Journal of Guidance, Control, and Dynamics 38 (11) (2015) 2057–2066.

[7] C. Chawla, P. Sarmah, R. Padhi, Suboptimal reentry guidance of a reusable launch vehicle using pitch plane maneuver, Aerospace Science and Technology 14 (6) (2010) 377–386.

[8] J. Qian, R. Qi, B. Jiang, Fault-tolerant guidance and control design for reentry hypersonic flight vehicles based on control-allocation approach, in: Proceedings of 2014 IEEE Chinese Guidance, Navigation and Control Conference, 2014, pp. 1624–1629.

[9] X. Lv, B. Jiang, G. Tao, X. Yao, An adaptive reconfigurable longitudinal trajectory control applied to the damaged space shuttle for approach and landing, in: Proceedings of 2014 IEEE Chinese Guidance, Navigation and Control Conference, 2014, pp. 1460–1465.

[10] T. E. Moore, Space shuttle entry terminal area energy management, Tech. Rep. NASA TM-104744, NASA Lyndon B. Johnson Space Center, Houston, TX, United States (Nov. 1991).

[11] K. Horneman, C. Kluever, Terminal area energy management trajectory planning for an unpowered reusable launch vehicle, in: AIAA Atmospheric Flight Mechanics Conference and Exhibit, 2004, pp. 5183–5201.

[12] C. Kluever, Terminal guidance for an unpowered reusable launch vehicle with bank constraints, Journal of Guidance, Control, and Dynamics 30 (1) (2007) 162–168.

[13] S. De Ridder, E. Mooij, Optimal longitudinal trajectories for reusable space vehicles in the terminal area, Journal of Spacecraft and Rockets 48 (4) (2011) 642–653.

[14] S. De Ridder, E. Mooij, Terminal area trajectory planning using the energy-tube concept for reusable launch vehicles, Acta Astronautica 68 (7) (2011) 915–930.

[15] S. De Ridder, E. Mooij, Optimal terminal area strategies and energy tube concept for a winged re-entry vehicle, in: AIAA Guidance, Navigation, and Control Conference, 2009, pp. 5769–5790.

[16] G. Morani, G. Cuciniello, F. Corraro, V. Di Vito, On-line guidance with trajectory constraints for terminal area energy management of re-entry vehicles, Proceedings of the Institution of Mechanical Engineers, Part G: Journal of Aerospace Engineering 225 (6) (2011) 631–643.

[17] X. J. Lan, L. Liu, Y. J. Wang, Online trajectory planning and guidance for reusable launch vehicles in the terminal area, Acta Astronautica 118 (2016) 237–245.

[18] G. H. Barton, A. C. Grubler, T. R. Dyckman, New methodologies for onboard generation of TAEM trajectories for autonomous RLVs, in: 2002 Core Technologies for Space Systems Conference, Citeseer, 2002, pp. 1–17.

[19] A. C. Grubler, New methodologies for onboard generation of terminal area energy management trajectories for autonomous reusable launch vehicles, Master's thesis, Massachusetts Institute of Technology (2001).

[20] J. Chartres, M. Graßlin, G. Schneider, Optimisation of the terminal flight phase for a future reusable launch vehicle, in: AIAA Guidance, Navigation, and Control Conference and Exhibit, 2005, pp. 6060–6072.

[21] L. X. Mu, X. Yu, Y. M. Zhang, P. Li, X. M. Wang, Trajectory planning for terminal area energy management phase of reusable launch vehicles, IFAC-PapersOnLine 49 (17) (2016) 462–467.

[22] K. Grantham, Adaptive critic neural network based terminal area energy management/entry guidance, in: 41st Aerospace Sciences Meeting and Exhibit, 2003, pp. 305–311.

[23] F. N. R. Salgueiro, E. de Weerdt, E. J. van Kampen, Q. Chu, J. Mulder, Terminal area energy management trajectory optimization using interval analysis, in: AIAA Guidance, Navigation, and Control Conference, 2009, pp. 5768–5788.

[24] J. H. Baek, D. W. Lee, J. H. Kim, K. R. Cho, J. S. Yang, Trajectory optimization and the control of a re-entry vehicle in TAEM phase, Journal of Mechanical Science and Technology 22 (6) (2008) 1099–1110.

[25] V. Morio, F. Cazaurang, A. Falcoz, P. Vernis, Robust terminal area energy management guidance using flatness approach, IET Control Theory & Applications 4 (3) (2010) 472–486.

[26] M. J. Poustini, R. Esmaelzadeh, A. Adami, A new approach to trajectory optimization based on direct transcription and differential flatness, Acta Astronautica 107 (2015) 1–13.

[27] C. Kluever, K. Horneman, J. Schierman, Rapid terminal-trajectory planner for an unpowered reusable launch vehicle, in: AIAA Guidance, Navigation, and Control Conference, 2009, pp. 5766–5779.

[28] B. N. Pamadi, G. J. Brauckmann, M. J. Ruth, H. D. Fuhrmann, Aerodynamic characteristics, database development, and flight simulation of the X-34 vehicle, Journal of Spacecraft and Rockets 38 (3) (2001) 334–344.

Onboard Guidance System Design for Reusable Launch Vehicles in the Terminal Area Energy Management Phase

Lingxia Mu[a,b], Xiang Yu[b], Youmin Zhang[b], Ping Li[a], Xinmin Wang[a]

[a] School of Automation, Northwestern Polytechnical University, Xi'an 710072, China
[b] Department of Mechanical, Industrial and Aerospace Engineering, Concordia University, Montreal H3G 1M8, Canada

Highlights

1) An onboard TAEM guidance system is designed for an unpowered RLV.
2) Constrained longitudinal profiles are generated by an iteration algorithm.
3) Longitudinal and lateral motions are integrated by an onboard management scheme.
4) Trajectory tracking laws are developed considering in-flight situations.
5) The effectiveness of the guidance system is verified by several simulation tests.